Supporting Information

Mechanistic interactions in polymer electrolyte fuel cell catalyst layer degradation

Navneet Goswami[1], Jonathan B. Grunewald[2], Thomas F. Fuller[2], and Partha P. Mukherjee[1, *]

[1]School of Mechanical Engineering, Purdue University, West Lafayette, IN 47907, United States

[2]School of Chemical and Biomolecular Engineering, Georgia Institute of Technology, Atlanta, GA 30332, United States

*Corresponding author: pmukherjee@purdue.edu (P. P. Mukherjee)

S1. Sensitivity of parameters on a cyclic voltammogram profile:

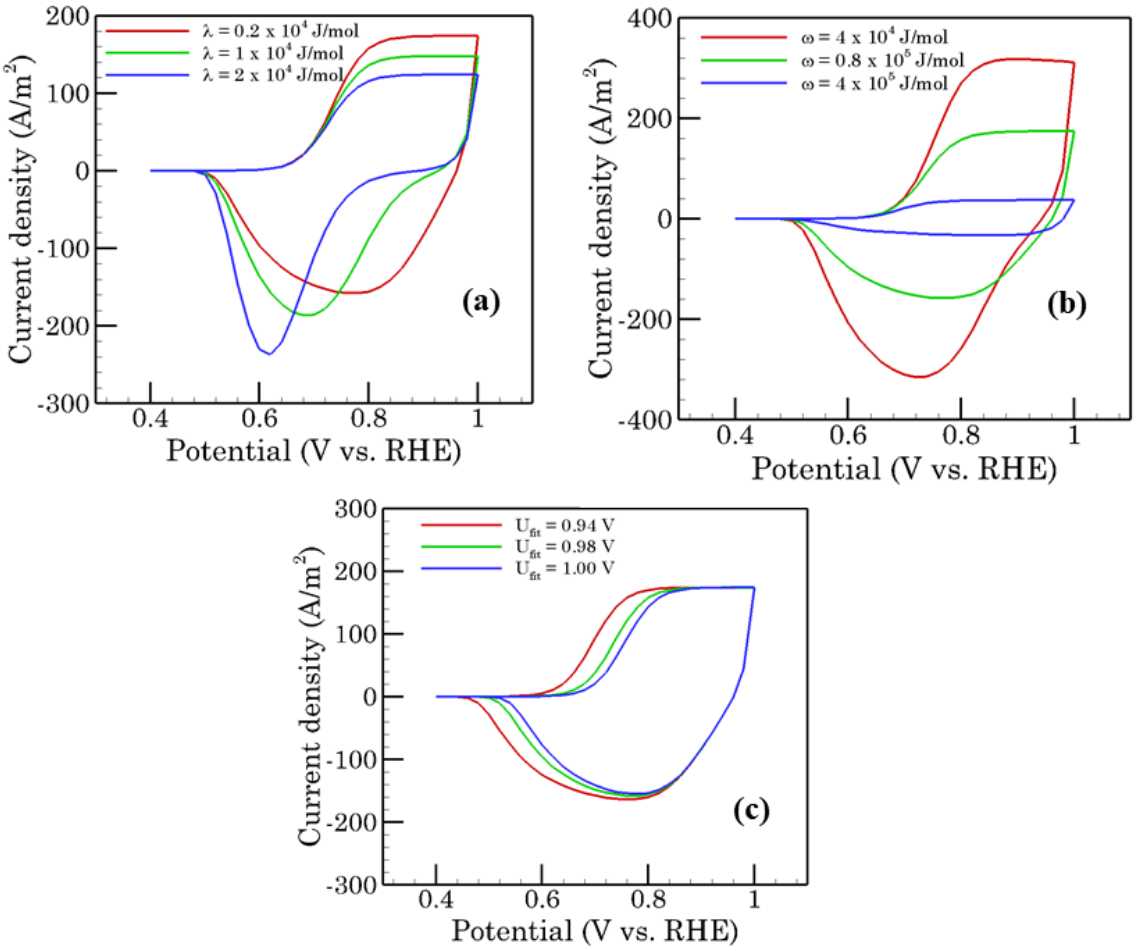

Fig. S1. Influence of kinetic parameters: (a) PtO-dependent kinetic barrier constant (λ), (b) Pt oxide-oxide interaction energy (ω), and (c) bulk equilibrium voltage for the onset of Pt-O formation (U_{fit}) on the shape of a cyclic voltammogram

The effect of thermo-kinetic parameters on the shape of a cyclic voltammogram (CV) corresponding to the initial durability cycle is shown in Fig. S1. The parameters of interest chosen in this analysis have been proved to majorly dictate the characteristics of a CV and emerge to be important while fitting to experimental data. Three values each of the PtO-

dependent kinetic barrier constant $\left(\lambda = 0.2\times10^4, 1\times10^4, 2\times10^4 \text{ J/mol}\right)$, Pt oxide-oxide interaction energy $\left(\omega = 4\times10^4, 0.8\times10^5, 4\times10^5 \text{ J/mol}\right)$, and bulk equilibrium voltage for the onset of Pt-O formation $\left(U_{fit} = 0.94, 0.98, 1 \text{ V}\right)$ have been considered. The baseline values $\left(\lambda = 0.2\times10^4 \text{ J/mol}, \omega = 0.8\times10^5 \text{ J/mol}, U_{fit} = 0.98 \text{ V}\right)$ constitute the curve with the best fit to the experimental CV data as seen in Fig. 2(a) in the main text. As observed in Fig. S1(a), tuning the PtO-dependent kinetic barrier constant to higher values decreases the anodic leveling current and shifts the cathodic peak towards the left, i.e., lower cathodic peak voltages and a higher absolute value of the cathodic peak currents. Change in the Pt oxide-oxide interaction energy (Fig. S1(b)) is manifested either in the form of expansion or contraction of the curve thereby changing the shape of the CV. Finally, bulk equilibrium voltage for the onset of Pt-O formation indicates the magnitude of the reversible open circuit potential (Fig. S1(c)) and accordingly modulates the point in the anodic half at which the oxidation of the catalyst particles is most likely to start (low value of U_{fit} means the early onset of PtO formation).

S2. Extraction of statistical parameters from an experimental particle size distribution (PSD):

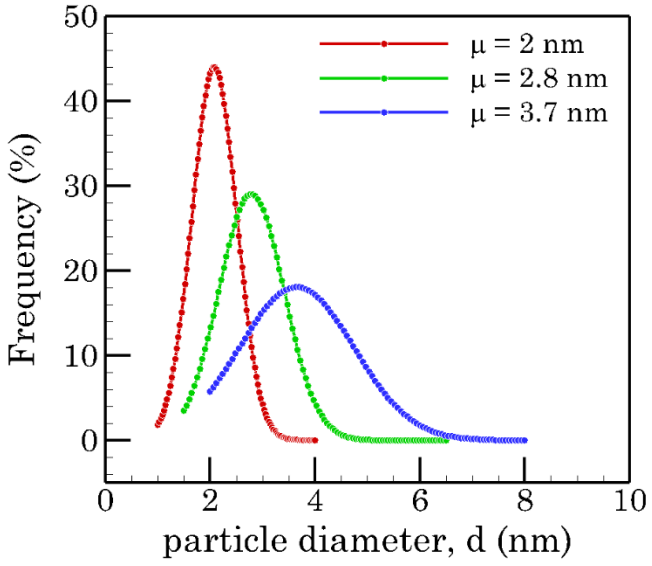

Fig. S2. The particle size distributions (PSDs) considered in the present study

An initial particle size distribution (PSD) serves as model input. The distribution consists of a finite number of particle groups, categorized by the particle radius and number density (number of particles) within each group. Based on an experimental transmission electron microscopy (TEM) dataset[1], analysis is performed to derive the relevant statistical parameters by fitting a Gaussian distribution. Fig. S2 shows the assumed PSD discretized into 100 groups with a mean particle radius (μ) of 2 nm (red curve), 2.8 nm (green curve), and 3.7 nm (blue curve),. The initial electrochemical active area (ECA) is assumed to be 55 m^2/g, which is the beginning of life ECA of the pristine membrane electrode assembly (MEA). At every time step, the particle groups are evolved (either coarsens or shrinks) as highlighted in the main text using the set of parameters enlisted in the Nomenclature section.

S3. Grid Independence test:

Results of the grid independence test are revealed in Fig. S3 which have been performed for a PSD with 2.8 nm mean particle radius, 20% ionomer volume fraction, and high temperature and fully humidified conditions (90℃ and 100% respectively). It is observed that N = 25 (x-direction) and M = 100 (y-direction) can be deemed to be a suitable selection as it neither sacrifices the computation accuracy while maintaining a balanced computational overhead. All the simulation results presented in the manuscript are for the aforementioned grid.

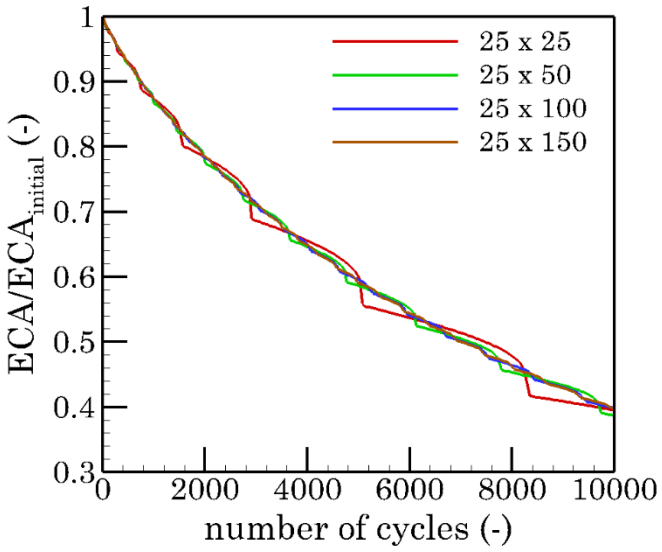

Fig. S3. Dependence of computational grid size on the transience of ECSA with cycling time

S4. Validation studies:

Fig. S4(a) shows the comparison of the simulated (from this work) and experimentally measured (from Bi and Fuller[2]) cathode cyclic voltammetry (CV) curves based on a potential cycle ranging from 0.4-1.0 V (vs. reference hydrogen electrode, RHE) with a scan rate of 50 mV/s at 60°C and fully humidified conditions. The CV current calculated as per Eq. S1 shows a good fit with that measured experimentally. The fitted thermo-kinetic parameters have been employed in all the simulations reported in this work. As seen in Fig. S4(b), the thermo-kinetic degradation model has been validated against experimental work of Harzer et al.[3] for triangular-wave potential cycling from 0.6-1.0 V under H_2-N_2 conditions for 10,000 cycles at 80°C and fully humidified conditions for two loading scenarios of the Pt catalyst - 0.1 and 0.4 mg/cm2. The simulation results accurately predict the transient profile of the change in ECA and mostly importantly, the loss in ECA after the end of 10,000 cycling sequences.

$$i = F\left(\pi d_{i,j}^2\right) Num_{i,j}\left(r_{net,Pt^{2+}} + r_{net,oxide}\right) L_{CCL} \tag{S1}$$

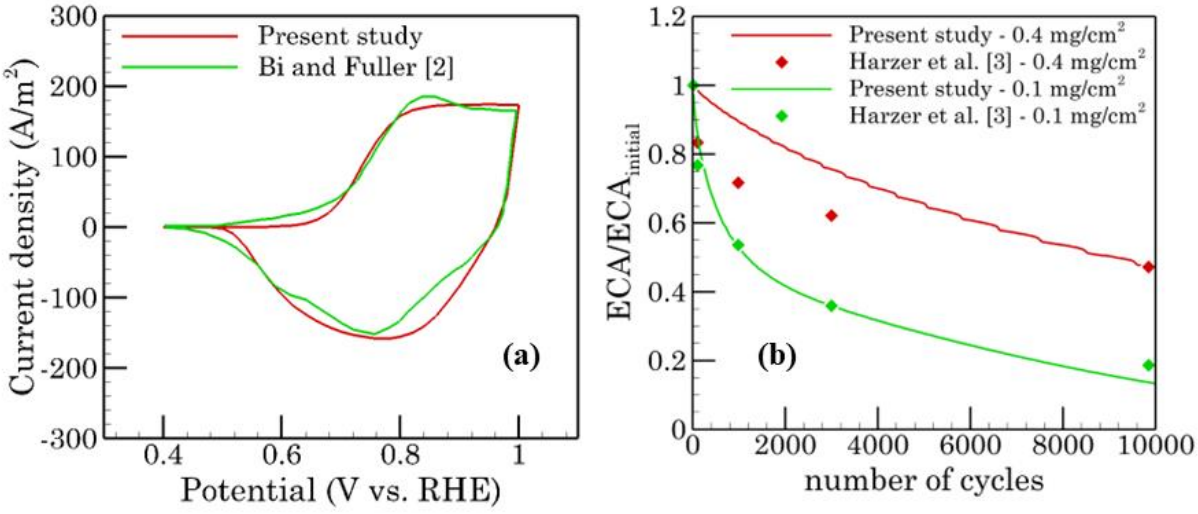

Fig. S4. Validation of the numerical code of the degradation model against literature data – (a) Cyclic Voltammetry (CV) profiles under 0.4-1.0 V potential cycling under H_2-N_2 conditions with Bi and Fuller[2], and (b) decay of electrochemical area under 0.6-1.0 V triangular-wave potential cycling under H_2-N_2 conditions for 10,000 cycles show agreement with Harzer et al.[3] for two loading scenarios of the Pt catalyst - 0.1 and 0.4 mg/cm^2

S5. Governing equations, boundary conditions employed in the reactive transport model:

Conservation of charge in Pt/C phase:

$$\frac{\partial}{\partial x}\left(\sigma_s^{eff}\,\frac{\partial \phi_s}{\partial x}\right) - j = 0 \tag{S2}$$

Conservation of charge in ionomer phase:

$$\frac{\partial}{\partial x}\left(\kappa_e^{eff}\,\frac{\partial \phi_e}{\partial x}\right) + j = 0 \tag{S3}$$

Conservation of gaseous oxygen in the pore phase:

$$\frac{\partial}{\partial x}\left(D_{\mathrm{O_2}}\,\frac{\varepsilon}{\tau}\frac{\partial c_{\mathrm{O_2}}}{\partial x}\right)+\ \frac{j}{4F}=0 \tag{S4}$$

Conservation of water vapor in the pore phase:

$$\frac{\partial}{\partial x}\left(D_{\mathrm{H_2O}}\,\frac{\varepsilon}{\tau}\frac{\partial c_{\mathrm{H_2O}}}{\partial x}\right)-\frac{j}{2F}=0 \tag{S5}$$

The system of coupled equations (S2-S5) needs to adhere to a set of boundary conditions as delineated below.

For the potential, ϕ_s in Pt/C phase:

$$\begin{aligned} &\text{Membrane-CCL interface}\ \ (x=0) && \frac{\partial \phi_s}{\partial x}=0 \\ &\text{CCL-GDL interface}\ \ (x=L_{CCL}) && -\sigma_s^{eff}\,\frac{\partial \phi_s}{\partial x}=I \end{aligned} \tag{S6}$$

For the potential, ϕ_e in ionomer phase:

$$\begin{aligned} &\text{Membrane-CCL interface}\ \ (x=0) && -\kappa_e^{eff}\,\frac{\partial \phi_e}{\partial x}=I \\ &\text{CCL-GDL interface}\ \ (x=L_{CCL}) && \frac{\partial \phi_e}{\partial x}=0 \end{aligned} \tag{S7}$$

For the concentration of gaseous oxygen, $c_{\mathrm{O_2}}$ in the pore phase:

$$\text{Membrane-CCL interface}\ \ (x=0) \qquad \frac{\partial c_{\mathrm{O_2}}}{\partial x}=0 \tag{S8}$$

CCL-GDL interface $(x = L_{CCL})$ $$c_{O_2} = c_{O_2}\Big|_{x=L_{CCL}}$$

For the concentration of gaseous oxygen, c_{H_2O} in the pore phase:

Membrane-CCL interface $(x = 0)$ $$-D_{H_2O}\frac{\varepsilon}{\tau}\frac{\partial c_{H_2O}}{\partial x} = N_{w,net}\Big|_{x=0}$$ (S9)

CCL-GDL interface $(x = L_{CCL})$ $$c_{H_2O} = c_{H_2O}\Big|_{x=L_{CCL}}$$

The oxygen concentration at the CCL–GDL interface ($x = L_{CCL}$) can be calculated by taking into account the drop from the constant gas concentration in the gas channel through the diffusion resistance in the GDL.

$$c_{O_2}\Big|_{x=L_{CCL}} = c_{O_2,\,inlet} - \frac{I}{4F}\frac{L_{GDL}}{\left(D_{O_2}\frac{\varepsilon}{\tau}\right)_{GDL}}$$ (S10)

Gaseous oxygen ingresses through the secondary pores and finally penetrates through the thin ionomer film (thickness is denoted as $\hat{t}$) that covers the catalyst particles and consequently observes a local diffusion resistance. A concentration jump exists at the pore-ionomer interface due to the application of Henry's law as seen in Eq. S11. The oxygen reaching the available reaction sites can be calculated using Eq. S12 by including the effect of the film resistance offered by the ionomer.

$$c_{O_2}^{ionomer\ surface} = \frac{c_{O_2}}{H_{O_2}} \tag{S11}$$

$$c_{O_2}^{reaction\ site} = c_{O_2}^{ionomer\ surface} - \left(\frac{I}{4F}\right)\left(\frac{\hat{t}}{D_{O_2}^{ionomer}}\right) \tag{S12}$$

It must be pointed out that the bulk value of proton conductivity of the ionomer phase $\left(\kappa^{bulk}\right)$ (units of S/m), Henry's constant $\left(H_{O_2}\right)$ (units of Pa-m^{3}mol^{-1}), and oxygen diffusivity through the ionomer $\left(D_{O_2}^{ionomer}\right)$ (units of m^2/s) are a function of water content (λ) which further depends on the water activity, *a*, as per the experimental correlation shown in Eq. S16.

$$\kappa_e^{bulk} = 100\exp\left[1268\left(\frac{1}{303}-\frac{1}{T}\right)\right]\left(0.005139\lambda - 0.00326\right) \tag{S13}$$

$$D_{O_2}^{ionomer} = 1.3926\times10^{-10}\,\lambda^{0.708}e^{\left\{\frac{T-273.15}{106.65} - 1.6461\times10^{-10}\,\lambda^{0.708} + 5.2\times10^{-10}\right\}} \tag{S14}$$

$$H_{O_2} = 0.1552e^{\left(14.1 + 0.0302\lambda - \frac{666}{T}\right)} \tag{S15}$$

$$\lambda = \begin{cases} 0.043 + 17.81a - 39.85a^2 + 36a^3 \ \text{ for } \ 0 < a \le 1 \\ 14 + 1.4\left(a-1\right) \ \text{ for } \ 1 < a \le 3 \end{cases} \tag{S16}$$

The water activity, *a* depends on the local variation of water vapor concentration within the CCL and can be approximated as:

$$a = \frac{c_{H_2O}}{c_{H_2O}^{sat}} \tag{S17}$$

A balance between the fluxes resulting from electro-osmotic drag and back diffusion gives the net water flux at the membrane-CCL interface ($x = 0$) in Eq. S18. In this work, the magnitude of the water transport coefficient (α) is considered as 0.2. Invoking the diffusion resistance through the GDL, the concentration for water vapor at the CCL-GDL boundary ($x = L_{CCL}$) can be evaluated (Eq. S19). The net water flux at the CCL-GDL interface (Eq. S20) can be determined by adding the generation term to the interfacial flux in Eq. S18.

$$N_{w,net}\Big|_{x=0} = N_{w,electroosmotic\ drag} - N_{w,back\ diffusion} = \alpha \frac{I}{F} \tag{S18}$$

$$c_{\mathrm{H_2O}}\Big|_{x=L_{CCL}} = c_{\mathrm{H_2O},\ inlet} + \quad N_{w,net}\Big|_{x=L_{CCL}} \frac{L_{GDL}}{\left(D_{\mathrm{H_2O}} \frac{\varepsilon}{\tau}\right)_{GDL}} \tag{S19}$$

$$N_{w,net}\Big|_{x=L_{CCL}} = N_{w,net}\Big|_{x=0} + N_{w,production} = \alpha \frac{I}{F} + \frac{I}{2F} = (2\alpha + 1)\frac{I}{2F} \tag{S20}$$

The mole fractions of the multi-component species in addition to their corresponding concentration values at the channel inlet can be computed based on the operating conditions (relative humidity, pressure, temperature) as highlighted in Eqs. (S21-S27).

$$c_{\mathrm{H_2O},\ inlet} = RH.c^{sat}_{\mathrm{H_2O}} \tag{S21}$$

$$c^{sat}_{\mathrm{H_2O}} = \frac{p^{sat}_{\mathrm{H_2O}}}{RT} \tag{S22}$$

$$\sum x_i = 1 \tag{S23}$$

$$x_{H_2O} = RH.\frac{p^{sat}_{H_2O}}{p} \quad \text{(S24)}$$

$$x_{O_2} = 0.21\left(1 - x_{H_2O}\right) \quad \text{(S25)}$$

$$x_{N_2} = 0.79\left(1 - x_{H_2O}\right) \quad \text{(S26)}$$

$$c_{O_2,\,inlet} = x_{O_2}\frac{p}{RT} \quad \text{(S27)}$$

In this study, the combined diffusion coefficients of gaseous oxygen and water vapor (Eq. S28) are based on a harmonic averaging of the coefficients arising from Knudsen diffusion (as per Eq. S29) and Binary diffusion (as per Eq. S30). The reference pressure (p_o) and reference temperature (T_o) are taken as 1 atm and 273 K respectively.

$$D_i = \left(\frac{1}{D_{K,i}} + \frac{1}{D^g_{b,i}}\right)^{-1} \quad \text{(S28)}$$

$$D_{K,i} = \left(\frac{2}{3}\right)\left(\frac{8RT}{\pi M_k}\right)^{\frac{1}{2}} r_p \quad \text{(S29)}$$

$$D^g_{b,i}\left(T, p\right) = D^g_{b,i,o}\left(\frac{T}{T_o}\right)^{\frac{3}{2}}\left(\frac{p_o}{p}\right) \quad \text{(S30)}$$

The correlation for exchange current density in addition to bulk values of diffusivities and electronic conductivity have been taken from Goswami et al.[4]

S6. Evolution of the particle size distribution (PSD):

The particle size distribution in the form of number density, or equivalently, the number of particles per unit volume have been displayed for the pristine and EOL electrode for two scenarios – (a) 80°C, 60% RH (similar conditions as in Figure 2 of the manuscript) and, (b) 60°C, 20% RH. The broadening of the PSD towards the left at the EOL stage reveals the dissolution dependence of the particle diameters towards a limiting case where the number density drops to zero (Eq. 30 from the manuscript). Further, the inset figures also show that the PSD slightly shifts towards the right with the tail approaching larger particle sizes which is a manifestation of the redeposition phenomena that results in particle coarsening. It must also be mentioned that the particle coarsening is a bit more prominent under low humidity conditions (scenario (b)). Furthermore, when compared to coarsening, dissolution is the more significant degradation mode also observed in Baroody and Kjeang[5].

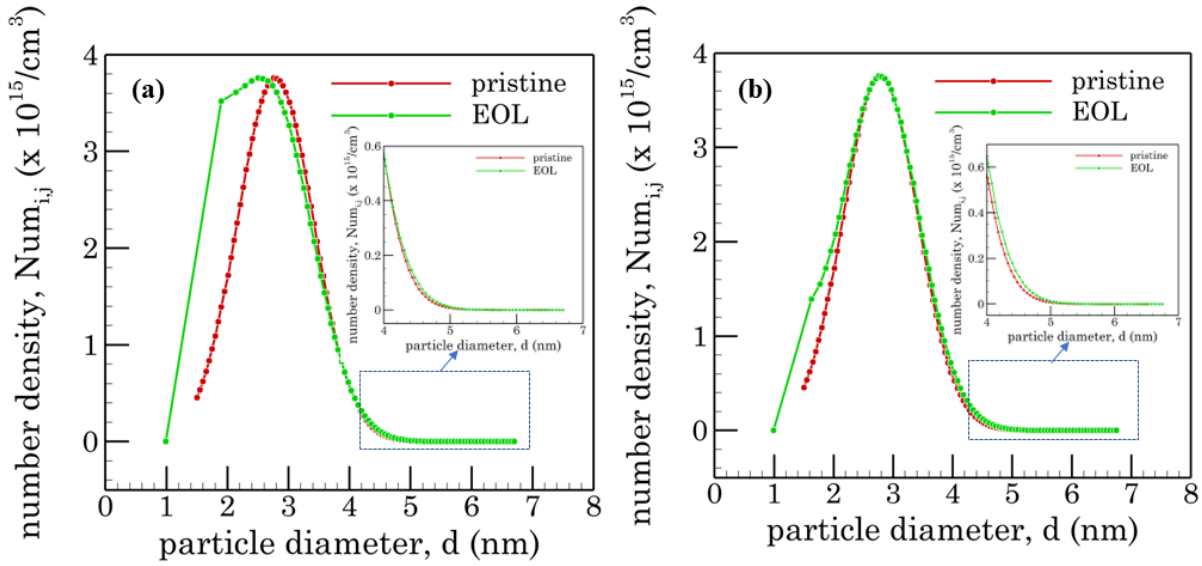

Fig. S5. The particle size distributions (PSDs) for the pristine and EOL electrode for two scenarios – (a) 80°C, 60% RH and, (b) 60°C, 20% RH

Nomenclature:

Symbol	Quantity	Description
ν_1	1.0×10^4 Hz	dissolution attempt frequency
ν_2	6.0×10^6 Hz	forward/backward dissolution rate factor
Γ	2.2×10^{-9} mol/cm^2	platinum surface site density
$\bar{H}_1$	4.7×10^4 J/mol	platinum dissolution activation enthalpy under fully humidified conditions
β_1	0.5	Butler−Volmer transfer coefficient for Pt dissolution
n_1	2	electrons transferred during Pt dissolution
$c_{Pt^{2+}}^{ref}$	1.0 mol/L	reference Pt^{2+} concentration
U_{eq}	1.188 V	thermodynamic bulk equilibrium voltage for platinum dissolution
ν_1^*	14.0×10^4 Hz	forward platinum oxide formation rate constant
ν_2^*	16.0×10^{-2} Hz	backward platinum oxide formation rate constant
$\bar{H}_2$	1.8×10^4 J/mol	partial molar oxide formation activation enthalpy (zero coverage)
$\beta_{2,a}$	0.5	anodic transfer coefficient for platinum oxide formation
$\beta_{2,c}$	0.35	cathodic transfer coefficient for platinum oxide formation
n_2	2	electrons transferred during platinum oxide formation
pH	0	system pH
λ	0.2×10^4 J/mol	platinum oxide-dependent kinetic barrier constant
U_{fit}	0.98 V	thermodynamic bulk equilibrium voltage for platinum oxide formation
ω	0.8×10^5 J/mol	platinum oxide−oxide interaction energy
γ_{Pt}	2.37×10^{-4} J/cm^2	surface tension of platinum
γ_{PtO}	1.0×10^{-4} J/cm^2	surface tension of platinum oxide
Ω_{Pt}	9.26 cm^3/mol	molar volume of platinum
Ω_{PtO}	14.97 cm^3/mol	molar volume of platinum oxide
ρ_{Pt}	21.09 cm^3/mol	density of platinum
$D_{Pt^{2+}}$	4.0×10^{-6} cm^2/s	diffusion coefficient of Pt^{2+} through the ionomer
L_{CCL}	10 μm	electrode thickness
T	60°C/ 80°C/ 90°C	Temperature
RH	20%/ 60%/ 100%	Relative humidity
$\varepsilon_{ionomer}$	0.1/ 0.15/ 0.20	volume fraction of the ionomer

List of Abbreviations:

PEFC	Polymer Electrolyte Fuel Cell
Pt	Platinum
ORR	Oxygen Reduction Reaction
ECA	Electrochemical Active Area
AST	Accelerated Stress Test
RH	Relative Humidity
MEA	Membrane Electrode Assembly
PSD	Particle Size Distribution
UPL	Upper Potential Limit
CCL	Cathode Catalyst Layer
GDL	Gas Diffusion Layer
GSA	Geometric Surface Area
EOL	End Of Life
CV	Cyclic Voltammetry

References:

1 D. J. S. Sandbeck, D. J. S. Sandbeck, M. Inaba, J. Quinson, J. Bucher, A. Zana, M. Arenz, M. Arenz and S. Cherevko, *ACS Applied Materials and Interfaces*, 2020, **12**, 25718–25727.

2 W. Bi and T. F. Fuller, *Journal of Power Sources*, 2008, **178**, 188–196.

3 G. S. Harzer, J. N. Schwämmlein, A. M. Damjanović, S. Ghosh and H. A. Gasteiger, *Journal of The Electrochemical Society*, 2018, **165**, F3118–F3131.

4 N. Goswami, A. N. Mistry, J. B. Grunewald, T. F. Fuller and P. P. Mukherjee, *Journal of The Electrochemical Society*, 2020, **167**, 084519.

5 H. A. Baroody and E. Kjeang, *Journal of The Electrochemical Society*, 2021, **168**, 044524.